Taylor & Francis
Taylor & Francis Group

Science and Technology of Advanced Materials: Methods

ISSN: (Print) (Online) Journal homepage: www.tandfonline.com/journals/tstm20

# Exploring high-symmetry structures in non-Cartesian coordinates: preparation and characteristics of cylindrically symmetric-rotating crystals

**Bo Da, Long Cheng, Xun Liu, Kunji Shigeto, Zihang Zhang, Kazuhito Tsukagoshi, Toshihide Nabatame, Zejun Ding, Jiangwei Liu, Hideki Yoshikawa & Shigeo Tanuma**

**To cite this article:** Bo Da, Long Cheng, Xun Liu, Kunji Shigeto, Zihang Zhang, Kazuhito Tsukagoshi, Toshihide Nabatame, Zejun Ding, Jiangwei Liu, Hideki Yoshikawa & Shigeo Tanuma (2024) Exploring high-symmetry structures in non-Cartesian coordinates: preparation and characteristics of cylindrically symmetric-rotating crystals, Science and Technology of Advanced Materials: Methods, 4:1, 2406743, DOI: 10.1080/27660400.2024.2406743

**To link to this article:** https://doi.org/10.1080/27660400.2024.2406743



Published online: 08 Oct 2024.

SCIENCE AND TECHNOLOGY OF ADVANCED MATERIALS: METHODS
2024, VOL. 4, NO. 1, 2406743
https://doi.org/10.1080/27660400.2024.2406743



# Exploring high-symmetry structures in non-Cartesian coordinates: preparation and characteristics of cylindrically symmetric-rotating crystals

Bo Da[a], Long Cheng[b], Xun Liu[a,b], Kunji Shigeto[c], Zihang Zhang[b], Kazuhito Tsukagoshi[d], Toshihide Nabatame[d], Zejun Ding[b], Jiangwei Liu[e], Hideki Yoshikawa[a] and Shigeo Tanuma[f]

[a]Center for Basic Research on Materials, National Institute for Materials Science, Tsukuba, Ibaraki, Japan; [b]Department of Physics, University of Science and Technology of China, Hefei, Auhui, P.R. China; [c]Electron Microscope Systems Design Department, Hitachi High-Tech Corporation, Hitachinaka, Ibaraki, Japan; [d]International Center for Materials Nanoarchitectonics (WPI-MANA), National Institute for Materials Science, Tsukuba, Ibaraki, Japan; [e]Research Center for Electronic and Optical Materials, National Institute for Materials Science, Tsukuba, Ibaraki, Japan; [f]Research Network and Facility Services Division, National Institute for Materials Science, Tsukuba, Ibaraki, Japan

**ABSTRACT**

Since their discovery in 1981, quasicrystals have challenged traditional crystallography, showcasing the diversity of material structures. Quasicrystals are ordered structures in higher-dimensional Cartesian coordinate systems projected into lower dimensions. Exploring whether materials can grow into high-symmetry ordered structures in different mathematical coordinate systems is an intriguing topic. This paper reports a new crystallization growth mode in InSiO thin films, exhibiting high symmetry in spherical and cylindrical coordinate systems, named cylindrical symmetric rotating crystals (CSRC). These crystals show rotational symmetry in their lattice structure, consistent with cylindrical symmetry. They are also part of spherical crystals, which theoretically have one of the highest symmetries. Theoretical predictions suggest that a two-dimensional slice of a spherical crystal in conventional grating mode SEM images will display relatively complete Kikuchi patterns due to the wave properties of incident electrons, unlike crystals or quasicrystals, which show surface morphology from the particle properties of incident electrons. We formed InSiO CSRC by heating InSiO amorphous films and observed relatively complete Kikuchi patterns that quantitatively relate to the incident electron beam direction and energy. These findings align with theoretical predictions, indicating that the Kikuchi patterns in SEM images result from Bragg diffraction through coherent electron scattering within the crystals. Quantitative analysis of these patterns provides information on the lattice structure, constants, crystal orientation, stress information, defect concentration, and Brillouin zone of the InSiO material. This method of obtaining microstructural information directly from SEM images applies only to CSRC, not to conventional or quasicrystal samples.

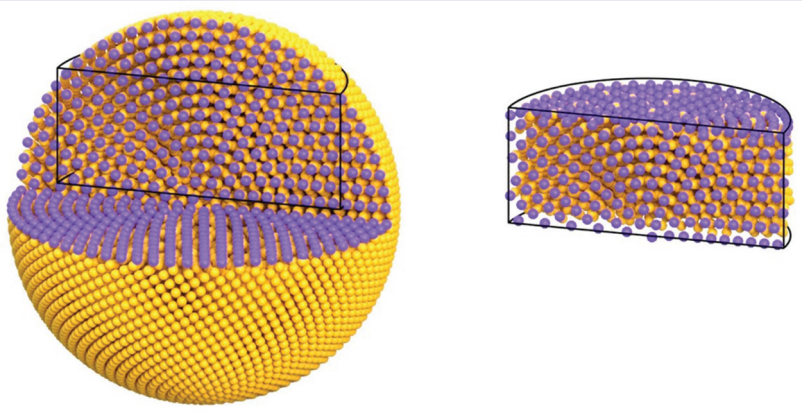

**IMPACT STATEMENT**

Unveiling a unique rotating crystal, this study expands the understanding of scanning electron microscopy (SEM) contrast mechanisms by simultaneously capturing real-space morphology and momentum-space lattice information in a single image.

**ARTICLE HISTORY**
Received 24 October 2023
Revised 6 September 2024
Accepted 16 September 2024

**KEYWORDS**
InSiO; cylindrically symmetric-rotating crystal; Kikuchi pattern; electron diffraction; SEM

**CONTACT** Bo Da DA.Bo@nims.go.jp Center for Basic Research on Materials, National Institute for Materials Science, Tsukuba, Ibaraki 305-0044, Japan

## 1. Introduction

When a sample material is observed using scanning electron microscopy (SEM), electrons interact with the surface, emitting an electronic signal containing a variety of diagnostic information. Surface morphology and sample composition are the most important factors affecting SEM imaging [1,2]; the basis of SEM image formation requires contrast between backscattered electrons, the most common types of which are morphology contrast [3–6] and composition/element contrast [7–10], applicable to almost all specimens. In addition, some special contrast mechanisms such as electric field [11,12], magnetic [13,14], electron charging [15,16] and proton gain [17–20] exist in certain types of materials and are closely related to specific material properties and are well explained by the particle nature of electrons. SEM also produces diffraction contrasts [21–27], such as electron backscatter diffraction (EBSD), which usually reflect structural information of the specimen, such as grain orientation, local texture, and phase identification/distribution. To observe the relatively complete diffraction pattern of a crystalline or polycrystalline sample with SEM, a different mode of operation is typically needed, to utilize the wave nature of the electrons.

However, theoretically, there exists a very special class of crystals that can exhibit unique diffraction contrast in standard SEM imaging mode. This class of crystals must possess continuous rotational symmetry and is named spherical crystals. Ideal spherical crystals have perfect spherical symmetry, meaning their atomic structure remains unchanged when rotated in any direction. They are one of the theoretically highest symmetry structures possible. In ideal spherical crystals, due to the continuous rotation of internal crystal orientation, their slices perpendicular to the radius will exhibit unique symmetry, theoretically predicted to display unique diffraction contrast in standard SEM imaging mode. In this paper, continuous symmetry refers to the property of a system where certain transformations, such as rotations or translations, do not alter the system's appearance or properties. However, when considering the atomic nature of crystals, true continuous symmetry is not achievable because atoms are arranged in a discrete lattice structure. Thus, while macroscopic observations may suggest continuous symmetry, at the atomic level, this symmetry is inherently limited by the discrete arrangement of atoms.

However, the spherical crystals discovered so far, or their slices as cylindrical symmetric rotating crystals (CSRCs) [28], as reported in spherical Se [29], $Fe_2O_3$ [30], $V_2O_3$ [31] fibers and $Cr_2O_3$ [31], $Ta_2O_5$ [32], Ge-Te, Tl-Se, and Cd-Te alloys [33], and single-crystal copper-iron alloys [34], have not been able to demonstrate unique diffraction contrast. In general, spherical grains are formed by a non-crystallographic branching mechanism, in which parent and daughter fibers do not have the same crystallographic orientation, with a misorientation angle between adjacent fibers usually between 0° and 15°. The growth mechanism of non-crystalline branches sets spherulites apart from other types of crystal formations and polycrystalline aggregates that exhibit round shapes. Thus, in these previously reported crystalline films composed of spherical grains, their local crystallographic orientation changes only slightly within the fibers, i.e. the crystal orientation rotates along the radial direction of the crystal. In contrast, the local crystalline orientation does not exhibit a continuous rotational behavior in the vertical direction of the fiber growth direction (i.e. tangential direction), because of the large variation in crystalline orientation among the spherically crystallized fibers.

Thus, the currently discovered spherical crystals and rotating crystals do not satisfy continuous symmetry in their overall structure and do not strictly belong to ideal spherical crystals. This also explains why there have been no reports of rotating lattice single crystals showing relatively complete Kikuchi patterns in SEM images. To observe Kikuchi patterns, rotating lattice single crystals must meet the requirement of continuous symmetry, specifically spherical symmetry.

In this work, we demonstrate the solid-state crystallization of pure InSiO amorphous films into CSRC structures by controlling the crystallization temperature, finding that InSiO gradually crystallizes at 300°C with the appearance of cylindrical crystal islands. In these two-dimensional cylindrical grains, the crystal orientation gradually shifts, both radially and tangentially, maintaining a pattern that conforms to cylindrical symmetry.

A relatively complete Kikuchi pattern can be observed in the SEM images of these crystals, in good agreement with theoretical predictions. Furthermore, by analyzing SEM images, atomic lattice information of the presented CSRCs are obtained, including lattice structure, lattice constant, crystal orientation, stress information, defect concentration, and Brillouin zone of this unique crystal material. Such detailed atomic lattice information typically cannot be obtained from conventional SEM imaging, which lacks atomic-level resolution.

## 2. Results and discussion

### 2.1. Principle of Kikuchi pattern in TEM image

Transmission Kikuchi Diffraction (TKD), alternatively known as transmission-electron backscatter diffraction (t-EBSD), represents a sophisticated methodology for nanoscale orientation mapping. It

facilitates the examination of microstructural attributes in thin specimens prepared for transmission electron microscopy (TEM), employing a scanning electron microscope (SEM). This approach has gained significant traction in the analysis of nano-crystalline substances, spanning oxides, superconductors, and an array of metallic alloys.

In TEM analysis, Kikuchi lines are observable in diffraction patterns from thick specimen regions experiencing multiple scatterings [35]. In contrast to diffraction spots that flicker with changes in crystal tilt, Kikuchi bands establish a structured orientation space with distinct intersections (referred to as zones or poles) and pathways connecting each intersection to the next. Discrete diffraction spots arise from the coherent scattering of the incident beam, while the formation of Kikuchi bands described through a biphasic process encompassing incoherent scattering of the primary beam followed by coherent scattering of these forward-scattered electrons. Furthermore, TKD has been employed for the analysis of fine-grained ultramafic peridotite samples within the SEM. The preparation of specimens for TKD analysis may be conducted utilizing conventional methodologies applicable to TEM [36].

In TKD analysis, a slender foil specimen is oriented perpendicularly to the electron flux within a scanning electron microscope. The electron flux is precisely focused on a small area of the specimen, causing the crystalline lattice of the specimen to diffract the traversing electrons. This diffraction pattern is subsequently captured by a detection apparatus and subjected to analytical procedures to ascertain the crystallographic orientation and microstructural characteristics of the specimen [37].

Convergent beam electron diffraction (CBED) is an additional TEM electron diffraction technique used to study Kikuchi bands. It involves employing a convergent or divergent electron beam (conical electron beam). First introduced in 1939 by Kossel and Möllenstedt [38], CBED is instrumental in determining the symmetries of point groups and space groups for crystal structure analysis.

### 2.2. Principle of Kikuchi pattern in SEM image

Two modes of operation in scanning electron microscopy (SEM) are utilized to capture comprehensive diffraction patterns. The first mode involves collecting backscattered electrons from various directions as they exit the sample surface, particularly when the incident electrons strike the sample at a significant angle. This mode, known as electron backscattered diffraction (EBSD), involves the incident electron beam entering the sample at a glancing angle and being scattered by the atoms within.

The second mode, employed for observing complete diffraction contrast, entails scanning the surface of a single crystal sample by varying the incidence direction of the electron beam. This results in a continuously changing angle about the crystal direction, causing the electron beam to diffract on the lattice at different locations on the sample surface and forming a Kikuchi pattern. This mode is referred to as the electron channeling pattern (ECP).

### 2.3. Cylindrical symmetric rotating crystals (CSRC)

Crystalline materials occupy a vital position in the fields of science and engineering, with their unique symmetry and structural characteristics being crucial for various applications. Traditional crystalline materials exhibit symmetry through the periodic repetition of atomic arrangements, i.e. the crystal remains invariant through translational operations in space, as shown in Figure 1(a). This translational symmetry in a three-dimensional Cartesian coordinate system is the core feature of traditional crystal structures and forms the foundation for understanding and studying crystalline materials. Part of a crystal's symmetry can also be described by its rotational axes, where the crystal appearance remains unchanged after rotating by specific angles around a point, reflecting its inherent order. For instance, a crystal's symmetry can be one-fold, two-fold, three-fold, four-fold, or six-fold, all of which can divide 360 degrees evenly, indicating a complete filling of a circular space.

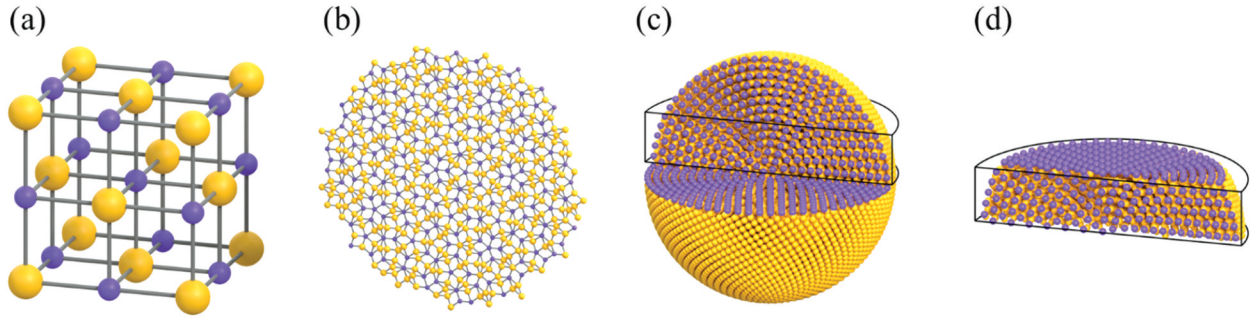


**Figure 1.** (a) Traditional crystals with a regular lattice structure (cubic structure), (b) quasicrystals that do not satisfy translational symmetry but exhibit long-range order, (c) spherical crystals that exhibit continuous rotational symmetry (with one-quarter removed for clarity), and (d) cylindrical symmetric rotating crystals as slices of ideal spherical crystals (with one-half removed for clarity).

The discovery of quasicrystals in 1981 challenged the conventional concept of symmetry in crystallography [39–41]. Unlike traditional crystals, quasicrystals do not possess periodic translational symmetry but instead exhibit a non-periodic long-range ordered arrangement, as shown in Figure 1(b). This regular yet complex arrangement disrupts the fundamental principle of 'periodicity' in traditional crystallography and exhibits symmetries such as five-fold and ten-fold, which are absent in conventional crystal structures. These special symmetries mean that the crystal appearance remains unchanged after rotations of 72 degrees or 36 degrees, which is impossible in traditional three-dimensional crystallography. Despite lacking traditional translational symmetry, quasicrystals still follow strict mathematical rules. Their structures can be described in higher-dimensional Cartesian coordinate systems and projected into lower dimensions [42]. This discovery demonstrated the diversity and complexity of material structures, expanding our understanding of materials science.

Therefore, exploring new materials that form high-symmetry ordered structures in other mathematical coordinate systems would significantly expand the current crystallographic framework. In theoretical research in materials science, researchers have predicted high-symmetry structures in various mathematical coordinate systems [43,44]. Among these, spherical symmetry structures are the most intriguing. Crystalline materials with spherical symmetry satisfy continuous rotational symmetry in spherical coordinates, making them one of the highest symmetry material structures theoretically [45]. Such spherical crystals not only exhibit beautiful symmetry mathematically but may also display unique physical properties. Figure 1(c) shows an ideal spherical crystal, whose symmetry and consistency in all directions make it a key target in theoretical research and practical applications [45]. Despite the perfect spherical symmetry of ideal spherical crystals, where atomic arrangements remain unchanged in any rotational direction, there have been no reports of synthesizing ideal spherical crystals to date.

Based on the concept of ideal spherical crystals, we propose a new crystalline structure named cylindrically symmetric rotating crystals (CSRC). CSRCs are thin slices cut from ideal spherical crystals along the direction perpendicular to the radius, as shown in Figure 1(d). Their symmetry lies primarily along the axial direction of the cylinder (the radial direction of the original spherical crystal) and the uniform distribution of atoms in each ring on the cut plane. This structure maintains its appearance and structure when rotated around the cylindrical symmetry axis, exhibiting significant rotational symmetry. Additionally, CSRCs retain the continuous rotational symmetry of ideal spherical crystals, leading to a continuous rotation of crystal orientation on the cut plane, which also satisfies cylindrical symmetry.

### 2.4. Kikuchi pattern using CSRC sample

While the SEM raster scan mode is used to gather information in the real space of the sample, the ECP and EBSD modes are employed to acquire information about the sample in momentum space. In this study, a unique sample configuration involving CSRCs, where the crystal direction continuously rotates at a local position, maintaining cylindrical symmetry with respect to the central position, was employed. This allowed for the observation of a complete Kikuchi pattern in a single SEM image acquired in raster scan mode.

The Kikuchi pattern observed in the SEM images is created by a similar mechanism as electron channeling patterns (ECPs). Based on our previously developed approach [46,47], a dynamical method is employed in this work to construct SEM patterns of CSRCs by simulating the diffraction processes of electrons in $In_2O_3$ single crystals with different incident directions. The simulation method will be given in a separate paper. Here, we make theoretical reconstructions of the experimental SEM images, using the observed crystal orientation distribution. In our simulations, we neglect fluctuations in crystal rotation speed for each crystal island, and use the average rotation speed, which is the uniform variation of the angle between the electron incidence direction and the lattice of the $In_2O_3$ single crystal.

Theoretical simulations can show how CSRC islands can produce complete Kikuchi patterns in SEM images. Figure 2 shows how the electron beam is scanned over a CSRC sample. Here, the local crystal orientations at different positions in the CSRC sample change slowly and continuously, and the local crystal orientation at any position on the CSRC, relative to the local crystal orientation at the center of the sample, satisfies cylindrical symmetry. When the electron beam is scanned over the CSRC, the change in angle $\theta$ between the incident electron beam and the local crystal orientation causes the variety of backscattered signal collected by the detector in the SEM. As the sample is excited, electrons undergoing backscattering and meeting the Bragg diffraction condition, expressed as $2d\sin\theta=\lambda$, undergo diffraction on a specific set of crystal planes within the sample. This interaction results in the formation of two conical diffraction patterns, each with a central axis perpendicular to the respective crystal planes, observable in SEM images. The intersection of these two conical surfaces with the receiving screen gives rise to a luminous band known as the Kikuchi band. At points A and B, the angle $\theta$ is equal to the same degree as $\theta_B$. Between A and B,

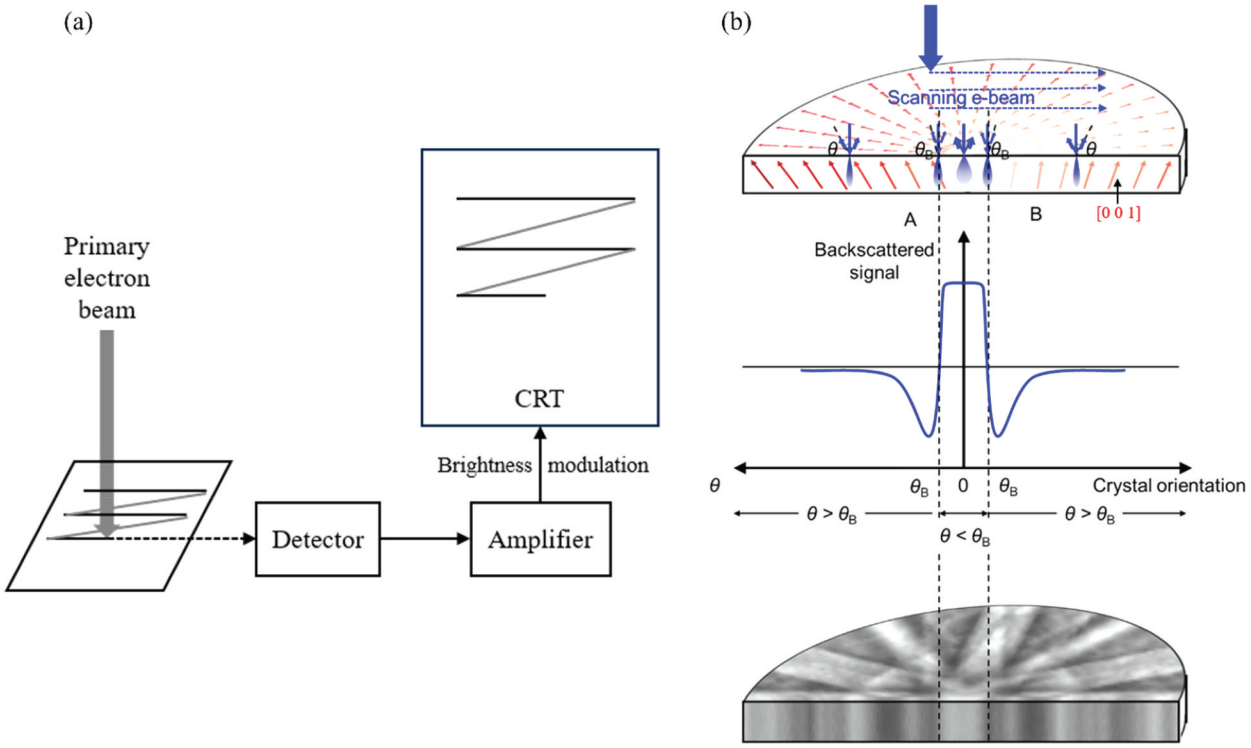


**Figure 2.** (a) Scanning electron microscope raster scanning schematic (b) schematic diagram of the variation of the angle $\theta$ between the incident electron beam and the local crystal orientation for an electron-incident CSRC sample, i.e. the angle between the red arrow and the blue arrow. As the electron beam is scanned along a line through the center of the CSRC, $\theta$ will vary between greater than $\theta_B$ to less than $\theta_B$. A and B in the figure are symmetrical positions corresponding to $\theta = \theta_B$. as shown in the lower part of the figure, the variation of $\theta$ is related to the variation of the intensity of the backscattered signal at the corresponding position on the CSRC. The two-dimensional CSRC satisfies cylindrical symmetry, and shows a Kikuchi pattern in the SEM backscattered electron image. The Kikuchi pattern here is a result of theoretical simulations. The red arrows are the crystal plane rotations of a CSRC, the blue cloud is the distribution of electron trajectories after the electron beam interacts with the material, and the darker and lighter colors represent different electron probability densities.

$\theta < \theta_B$, so an enhanced backscattered signal will be detected at these locations, while before and after A and B, $\theta > \theta_B$, so the backscattered signal will decrease.

Over the whole CSRC, the contrast in a 2D reconstruction of a typical 2D raster SEM survey contains contributions from several lattice planes together, and the resulting 'electron channel map' will show contrast bands from all planes. In this map, the width of each band is equal to twice the Bragg angle ($2\theta$) at the corresponding set of lattice planes, while the angle between different bands is equal to the angle between the sets of lattice planes from which those bands originate. Therefore, in conventional SEM mode, the incident electrons will diffract off the atomic lattice with different orientations at different landing positions even if the electron beam is scanned perpendicular to the surface of the sample. The resulting Kikuchi pattern is similar to that observed using EBSD.

### 2.5. SEM and EBSD images of CSRC sample

We use DC magnetron sputtering (Shibaura Mechatronics, CFS-4EP-LL i-miller) to prepare a 30 nm thick amorphous film on a sapphire substrate at room temperature. In the sputtering target, the main components are $In_2O_3$ and $SiO_2$ with Si/In ratio at 2.3 at.% [1 wt.% of $SiO_2/(In_2O_3 + SiO_2)$]. To obtain dynamic crystallographic images along a precisely fixed observation area, we use in situ SEM observations by heating the InSiO film to 300°C in the SEM chamber. The crystallization of InSiO through an annealing process is shown in Figure 3(a). With a gradual increase in temperature, the amorphous film gradually crystallizes, forming islands of circular crystals with diameters of approximately 1–2 μm and showing a distinct Kikuchi pattern. These islands of CSRCs grow from randomly distributed nucleation sites in the amorphous film, growing outwards two-dimensionally. In most cases, the nucleation sites are isolated, causing the islands of CSRCs to be separated from each other. In some cases, however, the growth of CSRC islands stops because of the presence of another crystallization point of an adjacent nucleus, forming CSRC islands close together. This is consistent with the typical island nucleation and growth process in thin films reported in the literature [48–51]. Figure 3(a) also shows that all these crystal islands exhibit a distinct Kikuchi-like diffraction pattern in the SEM images. These crystalline islands are observed to exhibit

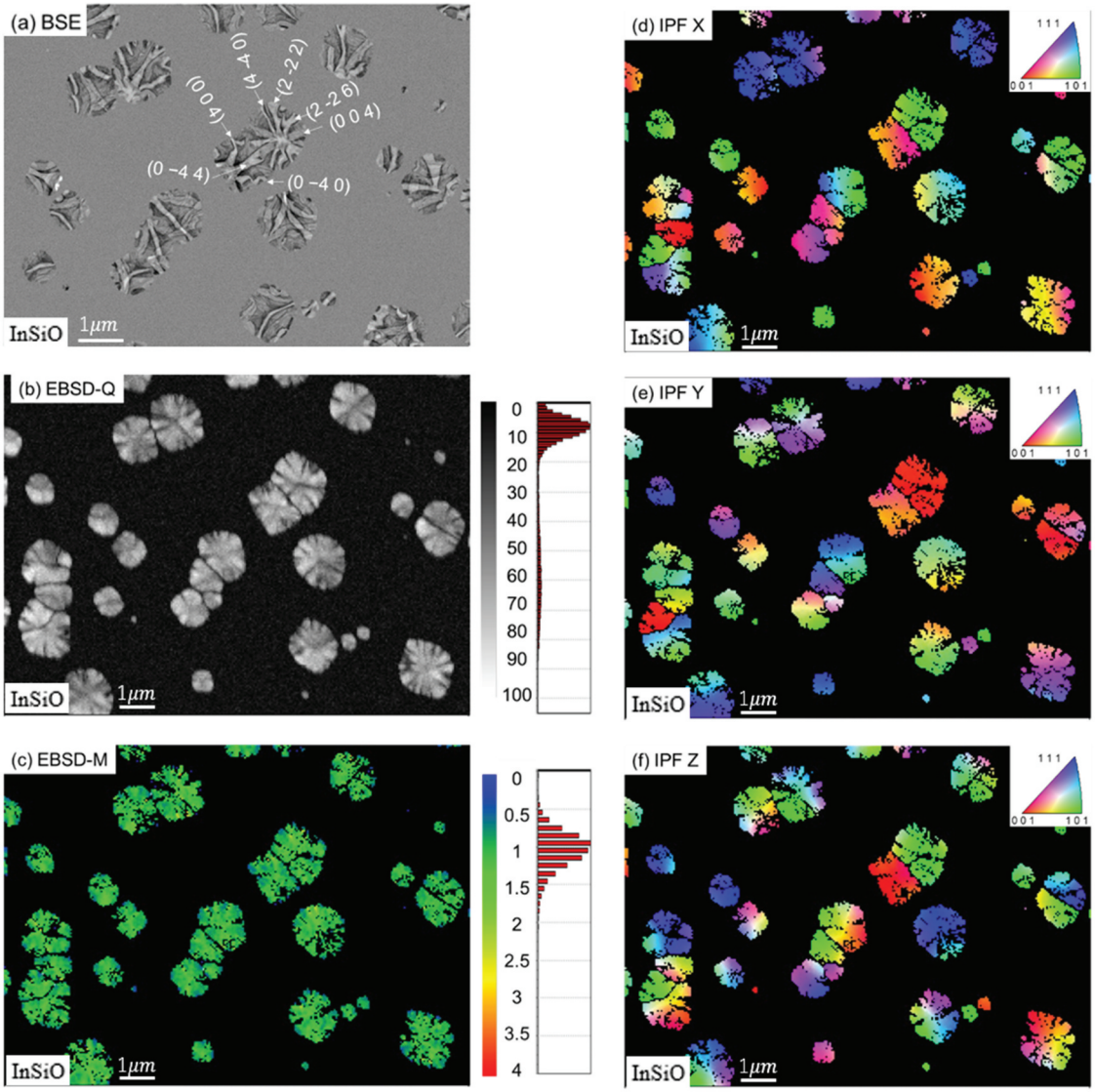


**Figure 3.** (a) SEM images of backscattered electron (BSE) detection of InSiO films observed during the crystallization of amorphous films at 300°C. (b) EBSD image quality map (EBSD-Q) with distribution of crystal quality, EBSD-Q is the sum of the detected peaks in the Hough transform, and describes the quality of an electron backscatter diffraction pattern. (c) EBSD misorientation map (EBSD-M) with the distribution of misorientation, describing the relative orientation of two grains with respect to each other, the unit is degree. And (d) x-axis, (e) y-axis, (f) z-axis Inverse Pole Figure (IPF), respectively.

different Kikuchi patterns, implying different crystallographic orientations of these crystal islands. All the observed Kikuchi patterns belong to cubic (bixbyite type) $In_2O_3$ structures.

Similar to previous studies [52], according to preferred nucleation orientations during crystallization, the observed Kikuchi patterns have several characteristic features. The preferred lattice orientation in $In_2O_3$ with [440] orientation is easily shown from the observed Kikuchi patterns, the characteristic features of which are shown in Figure 3(a). This orientation is derived from the $In_2O_3$ crystal Kikuchi pattern, which allows the assignment of indices to the Kikuchi band using the spherical projection of the Kikuchi pattern. The nuclei always appear in pairs while showing strong lattice curvature, corresponding to the small contour distances between the Kikuchi bands (hkl) and (-h-k-l). The SEM image in Figure 3(a) shows two sets of (−22-2) type planes, two sets of (−22-6) type planes, one (00–4) type plane and one (4–40) type plane, totalling six visible major Kikuchi bands. Different bandwidths are shown in different sets of Kikuchi bands, forming a bright 'pole' as a complex hexagon. Similarly, Kikuchi patterns with different characteristics for the [400], [222] zone axis are also shown in Figure 3(a).

These conditions are further confirmed by electron backscatter direction (EBSD) measurements as shown in Figure 3(c–e). The EBSD plot in the normal direction (EBSD-ND) is inhomogeneous. Figure 3(c) shows the different orientations within the CSRC islands with an EBSD-ND map using different colors. In each CSRC island, only one snowflake-like crystal 'grain' is apparent, and no obvious crystal misalignment boundaries can be observed.

Figure 3(b) shows the EBSD image quality (EBSD-Q). The EBSD-Q map shows that the crystal island have a snowflake-like mass distribution. The branched morphology of crystal mass originates from a relatively uniform central region, with the mass decreasing as larger features develop. This suggests that it is the density difference between the crystalline and amorphous InSiO films that forms the CSRC orientation during the crystallization process.

The EBSD misorientation (EBSD-M) map (Figure 3c) shows that the misorientation distribution in each CSRC island possess a pattern of snowflake outlines, within which the misorientation is almost identical at approximately 1°. This can also be determined by the distribution of misorientation shown in the right panel of Figure 3(c). This result implies that the crystal orientation shown by any pixel in the images of these CSRC islands is almost equal to that of the surrounding neighboring pixels.

Figure 4 shows, for three adjacent CSRC islands, quantitative information on the rotation of the local crystal orientation in five randomly selected directions. The variation of crystal orientation on the CSRC islands in the five selected directions is plotted in Figure 4. Although the three neighboring CSRC islands are of different sizes and have different crystal orientations, the rotation rates of the five randomly selected directions of the local crystal orientations are approximately equal. The average rotation rate of the crystal rotation angles is obtained with a linear fit. For this sample of CSRCs, the average crystal orientation rotation rate of the three adjacent CSRC islands is 16.62°/μm.

## 2.6. Analysis of SEM images

As previously determined, the observed Kikuchi patterns in secondary electron (SE) images can be attributed to the diffraction of electrons on the periodic atomic lattice of the sample. It is interesting to simultaneously observe the diffraction contrast and the morphology contrast in the SEM image. Here, the InSiO film is first annealed in air to 250°C and then transferred to the SEM chamber for further annealing to 300°C. Following this, many small bulbous protrusions with radii approximately 20–30 nm can be observed in the SEM images, caused by $In_2O_3$ nanocrystals separating out from the InSiO surface because of the interaction of amorphous $In_2O_3$ with water vapor in air. These $In_2O_3$ nanocrystals on the InSiO film surface provide a clear morphology contrast in both the BSE and SE images.

### 2.6.1. Analysis of symmetry

Figure 5 shows the BSE and SE images of three selected rotational crystal islands whose central region is in the [222], [400], and [440] crystal directions, respectively. It is clear that the characteristic Kikuchi pattern observed in both BSE and SE images originates from Bragg reflection from sets of lattice planes oriented perpendicular to the surface. In the CSRC island in the [222] direction (Figure 5a), three major Kikuchi bands visibly arise from the one set of (0–44)-type planes. As for the CSRC island in the [400] direction (Figure 5b), four major Kikuchi bands are visible from the two sets of (004)-type planes, and two sets of (0–44)-type planes. The CSRC island in the [440] direction (Figure 5c) shows six major Kikuchi bands due to the two sets of (–22-6)-type planes, two sets of (–22-2)-type planes, one (4–40)-type plane, and one (00–4)-type plane. In each CSRC island, different sets of Kikuchi bands process different bandwidths, and they intersect in a 'pole', forming a bright polygon with filigree-like internal

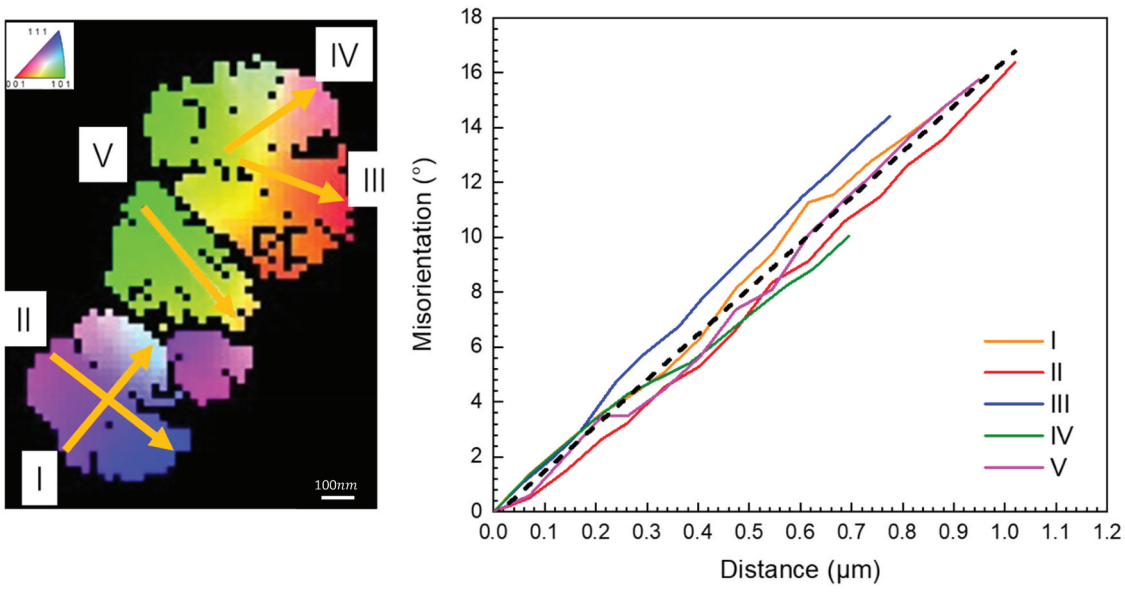


**Figure 4.** Crystal misorientation angle profiles measured along the yellow arrows inside the rotational crystallization island.

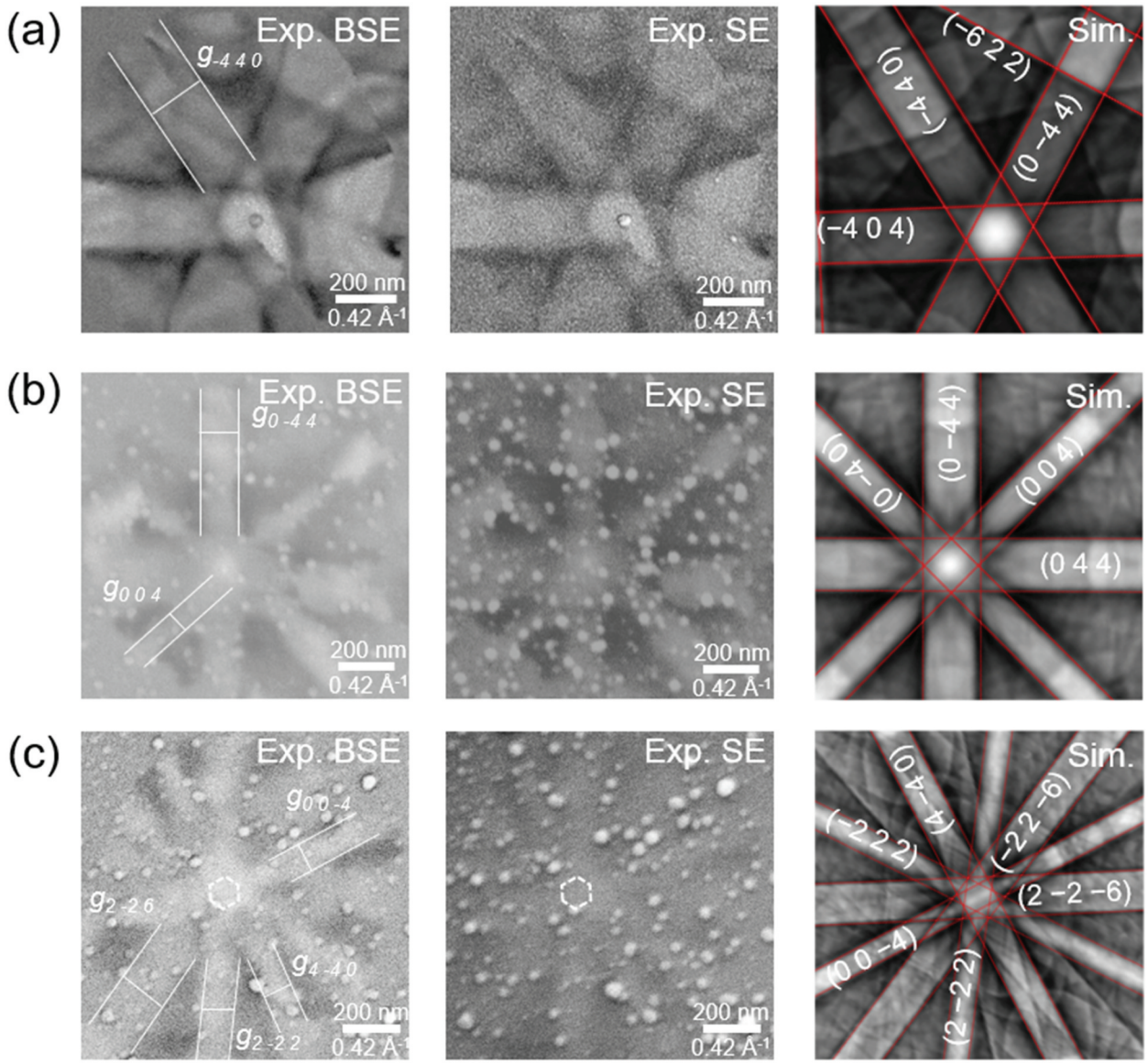


**Figure 5.** SEM images of the CSRC islands whose central region is (a) [222], (b) [400], and (c) [440] crystal directions, obtained by a backscattered electron (BSE) detector, secondary electron (SE) detector with incident electron energy of 15 keV, and corresponding simulated SEM images. The Miller indices are labeled on the simulated Kikuchi pattern. The red lines indicate the projections of lattice planes (hkl) shown by the labels. The size of the brillouin zone (brightest central polygon) in the projection plane for the CSRC island with a [440] direction is demonstrated in both measured SEM images and simulated images.

structures. The shape of the bright intersected region for the CSRC island in the [222] direction, and [400] direction are quite clear, while for the CSRC island in the [440] direction, it is relatively complex. The bright intersected region for the CSRC island in the [440] direction is a complex polygon composed of a bright central hexagon being the zone axis, i.e. the intersection region of the (004) Kikuchi band, (−22-6) Kikuchi bands, and (−22-6) Kikuchi bands, as well as six adjacent triangles being the intersection of two of these three bands. The sets of blurry lines originate from the higher-order reflection of the (−440) plane, flanking those major Kikuchi bands, and can be observed in the CSRC island in the [440] direction as a rounded bright region with a clear dark outline. The intersections between these blurry lines and the major Kikuchi bands, form some brighter nodes in those major bands.

A highly symmetric Kikuchi pattern can be observed in both SE and BSE images with almost the same features, while the contrast of the SE images is significantly lower than that of BSE images. This result implies that the diffraction information observed in SE images does not arise from the interaction when the SE is transported inside the crystal, but from the cascade SE produced by the backscattered electrons while traversing the crystal lattice. Therefore, the quantities for SE emitted from the different regions of the crystal surface are influenced by the local crystal direction where primary electrons land on different regions of the rotational crystal.

The simulated Kikuchi pattern agrees well with the experimentally observed Kikuchi pattern in the presented BSE and SE images, showing a good match with the bandwidths of different types of Kikuchi bands and the angles between them. The simulated pattern also effectively reproduces even the fine features in the intersection region of the Kikuchi bands, i.e. the bright complex polygons with filigree internal structures, as well as the rounded bright region and its dark outline.

Another notable point is that for the major Kikuchi bands observed in the CSRC island with the same direction, the widths all remain relatively consistent, even when they are far from the center of the CSRC island edges. One exception is for the (−404) plane in the rotational crystal island in the [222] zone axis because of the distorted lattice, as shown in Figure 5(a). This shows that the presented CSRC island has a highly consistent rotation speed, allowing further analysis of the Kikuchi pattern in the SEM image, to obtain useful physical quantities related to the crystal structure. It is generally not possible to obtain this information from SEM images of a conventional sample.

### 2.6.2. Analysis of lattice constant

According to the previous analysis for the CSRC sample, the Bragg angle can be determined by multiplying the rotation speed of the CSRC by the width of the Kikuchi band in the SEM images, as $2\theta_B = l \cdot d\Phi/dx$. Therefore, the lattice plane spacing is given by the expression, $d = \lambda/(l \cdot d\Phi/dx)$. In the presented SEM images, the band widths for each plane direction in the CSRC islands can be measured as listed in Table 1, together with the calculated corresponding lattice plane spacings.

Using the relation $a = d_{hkl}\sqrt{h^2 + k^2 + l^2}$, the calculated lattice constant a, determined from the lattice plane spacing is also listed in Table 1. The average value of the calculated lattice constants obtained for the CSRC islands with zone axis of [222], [400], and [440] are 8.49 Å, 13.03 Å ± 2.11 Å, and 11.61 Å ± 2.84 Å, respectively. The total average value of the calculated lattice constant is 11.57 Å ± 2.65 Å. These values are slightly larger than those obtained from the analysis of band width variations in the SEM image of the CSRC island with different incident electron energies.

### 2.6.3. Analysis of reciprocal lattice vector

Based on the determined lattice plane spacing $d$, the lengths $|g_{hkl}|$ of the reciprocal lattice vectors can be calculated by the formula, $g_{hkl} = \frac{2\pi}{d}$. Consequently, the reversed reciprocal lattice vectors for different planes in three different crystals can be calculated as listed in Table 1. According to the special relationship between the bandwidth of the Kikuchi band $l$ and the Bragg angle $\theta_B$ in the presented CSRC sample, i.e. $2\theta_B = l \cdot d\Phi/dx$, the lengths $|g_{hkl}|$ of the reciprocal lattice vectors can be rewritten as

$$g_{hkl} = \frac{2\pi}{d} = \frac{2\pi \, d\Phi/dx}{\lambda} l, \tag{1}$$

where, $d\Phi/dx$ is the rotation speed of the CSRC, and $\lambda$ is the electron wavelength. Because $d\Phi/dx$ is 20°/μm and $\lambda$ is 10 pm for electrons with 15 keV, the reversed reciprocal lattice vector, $g_{hkl}$ is only dependent on the bandwidth of Kikuchi band $l$, measured in the SEM images. Therefore, in the SEM image of the CSRC sample, each pixel corresponds to both the different spatial positions on the sample surface according to real-space coordinates and also to the different angle between the electron beam and a given crystal surface according to reciprocal-space coordinates, i.e. on a momentum scale. The transformation coefficient from the spatial scale to the momentum scale is, $\frac{2\pi d\Phi/dx}{\lambda}$. It is interesting to note the momentum scale of the presented SEM image of the CSRC sample at a given incident electron energy. For the incident electron energy of 15 keV, the transformation coefficient from the spatial scale to the momentum scale is, 0.0022 $Å^{-2}$. The presented SEM images are composed of 512 by 512 pixels, every pixel corresponds to 20.8 Å, 24.1 Å, 23.2 Å, in the real space coordinate and 0.046 $Å^{-1}$, 0.053 $Å^{-1}$, 0.051 $Å^{-1}$ in the momentum coordinate in the BSE and SE images of three rotational crystal islands at the zone axis of [222], [400], [440], respectively. This property makes it possible to determine the size of the two-dimensional Brillouin zone in the projection plane in momentum scale whose outline could be determined by extending prominent Kikuchi bands. Here, the side length of the two-dimensional Brillouin zone in the projection plane for the [440] crystal is marked in the BSE and SE

**Table 1.** The plane index, Bragg angle, bandwidth, plane spacing, reciprocal lattice vectors, calculated lattice constant, strain, Burgers vector and building-in geometrically necessary dislocation (GND) density in the observed CSRC island with zone axes of [222], [400], and [440]. Data were obtained by analyzing SEM images as shown in Figure 4.

| Zone Axis | h | k | l | Bragg angle (degree) | Bandwidth (nm) | Plane spacing (Å) | reciprocal lattice vectors ($Å^{-1}$) | calculated lattice constants (Å) | Strain | Burgers vector (Å) | GNDs density ($10^{13} m^{-2}$) |
|---|---|---|---|---|---|---|---|---|---|---|---|
| [222] | −4 | 4 | 0 | 1.91 | 190.6 | 1.5 | 4.19 | 8.49 | 0.52% | 24.00 | 14.57 |
| [400] | 0 | −4 | 4 | 1.40 | 140 | 2.04 | 3.08 | 11.54 | 0.52% | 32.64 | 10.73 |
| [400] | 0 | −4 | 0 | 0.79 | 78.8 | 3.63 | 1.73 | 14.52 | 0.52% | 29.04 | 12.04 |
| [440] | 0 | 0 | 4 | 1.06 | 105.59 | 2.71 | 2.32 | 10.83 | 0.52% | 21.67 | 16.14 |
| [440] | −2 | 2 | −6 | 1.66 | 166.15 | 1.72 | 3.65 | 11.42 | 0.52% | 37.87 | 9.23 |
| [440] | −2 | 2 | −2 | 1.14 | 113.89 | 2.51 | 2.50 | 8.70 | 0.52% | 15.07 | 23.21 |
| [440] | −4 | 4 | 0 | 1.05 | 104.37 | 2.74 | 2.29 | 15.50 | 0.52% | 43.84 | 7.97 |

images. The conventional SEM adopted for this special CSRC sample can be regarded as a momentum-microscopy like those reported by Fedchenko *et al.* [53].

### 2.6.4. Analysis of strain value

A simple estimation of the strain value in the CSRC is possible from the SEM image of this CSRC island, by assuming an elastic cylindrical bending of the CSRC in the radial direction. The maximum strain $\varepsilon$ of the surface film can be estimated according to Kolosov and Thölen [54], as

$$\varepsilon = \frac{t\theta_B}{l} = \frac{t\mathrm{d}\Phi/\mathrm{d}x}{2}, \tag{2}$$

where $\theta_B$ is the Bragg angle, $l$ is the bandwidth of the Kikuchi band, $t$ is the thickness of the CSRC film, and $\mathrm{d}\Phi/\mathrm{d}x$ is the average measured gradient of monotonously increasing misorientation angle for a CSRC. This can be expressed by the ratio of the angle spanned by the CSRC of the Kikuchi band to its bandwidth, as $\mathrm{d}\Phi/\mathrm{d}x = 2\theta_B/l$. Considering the film thickness is 30 nm, and $\mathrm{d}\Phi/\mathrm{d}x$ is 50°/μm the strain values calculated from each plane in three CSRC islands are consistent, as listed in Table 1. The presented strain value of CSRC islands is 0.52%, which is a relatively small value. According to Goh *et al.* [55], the microstrains in $In_2O_3$ NPs at different calcination temperatures (200°C, 300°C, 400°C, 500°C and 600°C) are 0.0736, 0.0944, 0.1144, 0.1500 and 0.1647, respectively. Our resulting strain value is far lower than the measured microstrain of $In_2O_3$ nanoparticles so, during annealing of the crystal, the inter force did not exceed the maximum strain value, so the crystal can rotate homogeneously without breaking, allowing the rotational crystal to form differently to normal crystals.

### 2.6.5. Analysis of building-in geometrically necessary dislocations (GNDs)

If we assume that the lattice rotation in the CSRC has a contribution from building-in geometrically necessary dislocations (GNDs) which accommodate a lattice curvature from a deformation gradient [56], we can approximately estimate the lower bound of the GND density from SEM images of the CSRC.

If one assumes a homogeneous distribution of GNDs in the CSRC, a lower bound estimation of the GND density can be found with [57]

$$\rho_{\mathrm{hom}} = \frac{\theta_{\mathrm{tot}}}{|b|\Delta x}, \tag{3}$$

where $\theta_{\mathrm{tot}}$ is the lattice bending angle over distance $\Delta x$, determined from dislocations with Burger's vector $b$ [58]. Therefore, for the CSRC, $\theta_{\mathrm{tot}}/\Delta x$ can be expressed as the ratio of the angle spanned by the CSRC of the Kikuchi band to its bandwidth, $2\theta_B/l$. Consequently, the formula can be rewritten as

$$\rho_{\mathrm{hom}} = \frac{2\theta_B}{|b|l} = \frac{\mathrm{d}\Phi/\mathrm{d}x}{|b|}, \tag{4}$$

substituting our experimental values of $\frac{\mathrm{d}\Phi/\mathrm{d}x}{|b|}$ taken from the SEM image, with $|b|$ being the size of the crystal axis along each plane direction, $|b| = \frac{a}{2}\sqrt{h^2+k^2+l^2}$ for bcc crystals as listed in Table 1. The GND densities calculated from each plane in three CSRC islands are listed in Table 1. The average value of the GND density obtained for the CSRC islands with zone axes of [222], [400], and [440] are $1.46\times10^{15}$ $m^{-2}$, $1.14\times10^{15}$ $m^{-2}$, $1.41\times10^{15}$ $m^{-2}$, respectively. Thus, the total averaged GND density is $1.34\times10^{15}$ $m^{-2}$. Such a large dislocation density has also been observed in nanostructured $In_2O_3$ thin film. For example, Dasari *et al.* [59] find that the dislocation density in $In_2O_3$ thin film is $4.25\times10^{15}$ $m^{-2}$ when the substrate temperature is approximately 350°C, and can be reduced to $1\times10^{15}$ $m^{-2}$ when the substrate temperature reaches 500°C.

It should be noted that the Kikuchi patterns in the experimental SEM data exhibit inhomogeneous bandwidths and shape distortions as shown in Figure 6, which are slightly different from those calculated in simulations. In the center of the CSRC island, the Kikuchi bandwidth and its direction are closer to the simulated results; when at the edge of the CSRC island, the fluctuations in the Kikuchi bandwidth and its direction become significantly larger. This means that in the actual CSRC, the rotation speed is approximately the same in the central region, while it becomes different in the local position away from the center of the CSRC island. Accordingly, by measure, the local bandwidth of the Kikuchi band in a given CSRC island, it is possible to determine the distribution of the Bragg angle, plane spacing, lattice constant, strain, and building-in GNDs density on the local region of a CSRC island where the Kikuchi pattern is presented. Figure 6 shows the measured distribution of bandwidth in the CSRC island with the zone axis of [400], as well as the corresponding distribution of Bragg angle, plane spacing, calculated lattice constant, strain, and building-in GND density.

## 3. Conclusions

We present a cylindrically symmetric rotating crystal (CSRC) film, prepared and observed using SEM and EBSD techniques. The discovery of CSRCs expands our understanding of material symmetry. Traditional crystals exhibit rotational symmetries ranging from one-fold to six-fold, all conforming to periodic structures. The discovery of quasicrystals challenged this concept by introducing five-fold, ten-fold, or other non-traditional symmetries. The emergence of CSRCs further extends the definition of symmetry, showcasing a unique, continuous rotational symmetry

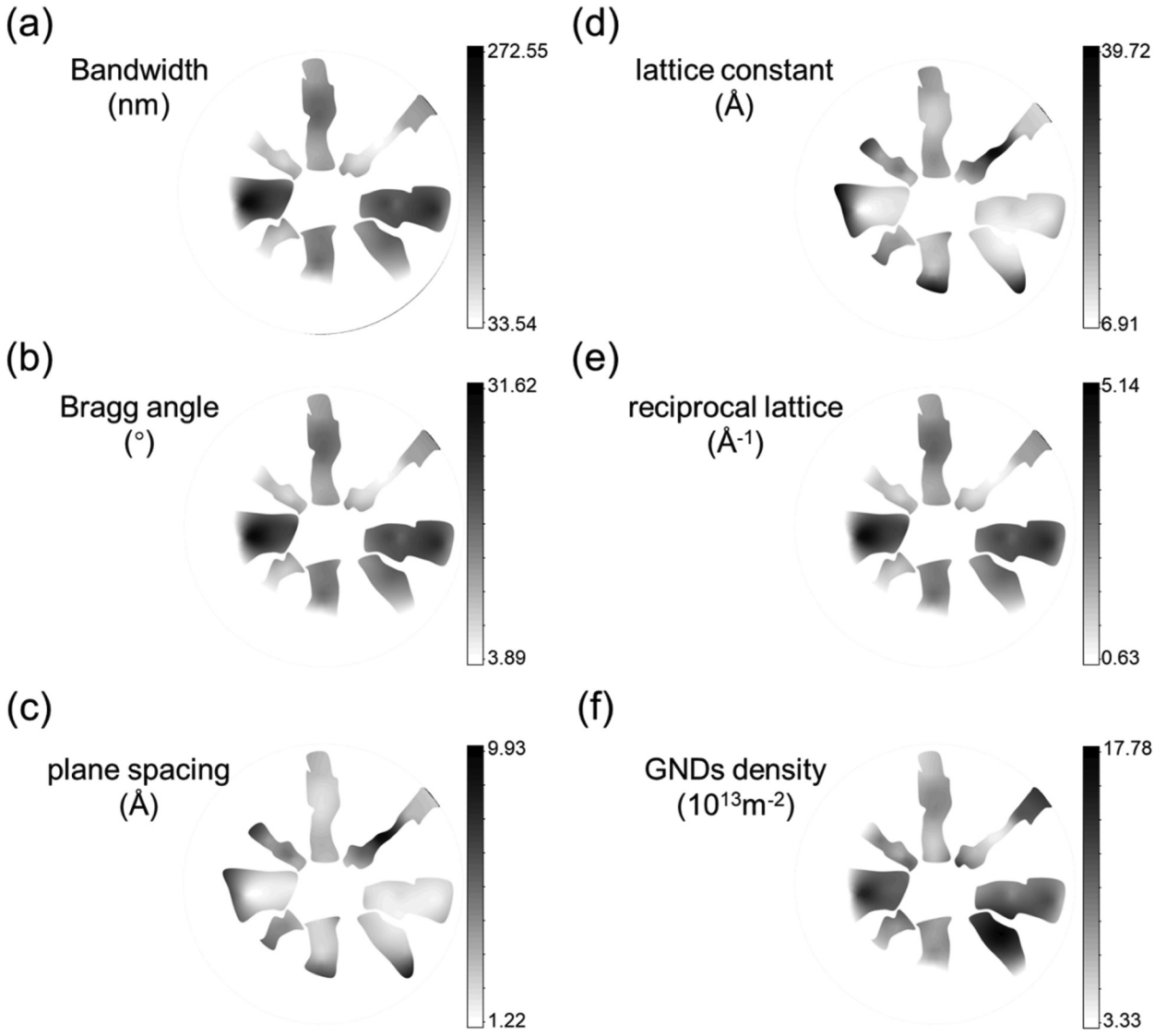


**Figure 6.** Distribution of bandwidth, Bragg angle, plane spacing, calculated lattice constant, strain, and building-in geometrically necessary dislocation (GND) density, determined by analysis of Kikuchi band widths in the CSRC island with a zone axis of [400].

based on cylindrical coordinates, which is unattainable in traditional crystals or quasicrystals. This material's local continuous rotational symmetry provides a unique SEM comparative case study. The observed SEM patterns can only be well interpreted by considering the wave-particle duality of electrons. In SEM normal mode, the CSRCs prepared here demonstrate not only the particle properties of the incident electrons in the surface morphology of the sample but also the wave properties of the incident electrons in the full Kikuchi pattern contrast. Based on these SEM images, we can obtain information related to the sample lattice, including the lattice constant of the InSiO material, crystal orientation, stress information of the crystal, defect concentration, and Brillouin zone. This information is not available from conventional non-atomic level resolution SEM imaging mode when using other types of crystal samples.

## Disclosure statement

No potential conflict of interest was reported by the author(s).

## Funding

This work was supported by the The Kurata Grants from The Hitachi Global Foundation and from The Iketani Science & Technology Foundation. J.H. was supported by the U.S. Department of Energy (DOE), Office of Science, Office of Basic Energy Sciences under Award DE-SC0019467. Z.J.D was supported by the National Key Research and Development Project [2019YFF0216404] and Education Ministry through "111 Project 2.0" [BP0719016]. All DFT calculations were performed on the Numerical Materials Simulator supercomputer at the National Institute for Materials Science. We are thankful for helpful discussions and suggestions from Dr. Takio Kizu.

## ORCID

Long Cheng http://orcid.org/0000-0001-9599-2257
Zejun Ding http://orcid.org/0000-0001-5767-1145

## Data availability statement

All data needed to evaluate the conclusions in this paper are presented in the paper and/or the Supplementary materials. Additional data related to this paper may be requested from the authors.

## References


[1] Zworykin VA, Hillier J, Snyder RL. A scanning electron microscope. ASTM Bull. 1942;117:15–23.

[2] Smith KCA, Oatley CW. The scanning electron microscope and its fields of application. Br J Appl Phys. 1955;6(11):391. doi: 10.1088/0508-3443/6/11/304

[3] Hejna J. Detection of topographic contrast in the scanning electron microscope at low and medium resolution by different detectors and detector systems. Scanning Microsc. 1994;8:1.

[4] Da B, Mao SF, Zhang GH, et al. Monte Carlo modeling of surface excitation in reflection electron energy loss spectroscopy spectrum for rough surfaces. J Appl Phys. 2012;112(3):034310. doi: 10.1063/1.4739491

[5] Da B, Mao SF, Zhang GH, et al. Influence of surface roughness on elastically backscattered electrons. Surf Interface Anal. 2012;44(6):647–652. doi: 10.1002/sia.4807

[6] Da B, Salma K, Ji H, et al. Surface excitation parameter for rough surfaces. Appl Surf Sci. 2015;356:142–149. doi: 10.1016/j.apsusc.2015.08.056

[7] Lloyd GE. Atomic number and crystallographic contrast images with the SEM: a review of backscattered electron techniques. Mineral Mag. 1987;51(359):3–19. doi: 10.1180/minmag.1987.051.359.02

[8] Allen LJ, D'Alfonso AJ, Findlay SD, et al. Elemental mapping in scanning transmission electron microscopy. J Phys Conf Ser. 2010;241:012061. doi: 10.1088/1742-6596/241/1/012061

[9] Da B, Mao SF, Ding ZJ. Validity of the semi-classical approach for calculation of the surface excitation parameter. J Phys Condens Matter. 2011;23(39):395003. doi: 10.1088/0953-8984/23/39/395003

[10] Da B, Sun Y, Mao SF, et al. Systematic calculation of the surface excitation parameters for 22 materials. Surf Interface Anal. 2013;45(3):773–780. doi: 10.1002/sia.5164

[11] Findlay D, Sasaki H, Matsumoto T, et al. Imaging of built-in electric field at a p-n junction by scanning transmission electron microscopy. Sci Rep. 2015;5(1):1–8. doi: 10.1038/srep10040

[12] Hachtel JA, Idrobo JC, Chi M. Sub-ångstrom electric field measurements on a universal detector in a scanning transmission electron microscope. Adv Struct Chem Imag. 2018;4(1):1–10. doi: 10.1186/s40679-018-0059-4

[13] Jones GA. Magnetic contrast in the scanning electron microscope: an appraisal of techniques and their applications. J Magn Magn Mater. 1978;8(4):263–285. doi: 10.1016/0304-8853(78)90096-3

[14] Kotera M, Katoh M, Suga H. Observation technique of surface magnetic structure using type-I magnetic contrast in the scanning electron microscope. Jpn J Appl Phys. 1995;34(12S):6903. doi: 10.1143/JJAP.34.6903

[15] Li C, Da B, Ding ZJ. Monte Carlo study on the surface potential measurement using the peak-shift method. Appl Surf Sci. 2020;504:144138. doi: 10.1016/j.apsusc.2019.144138

[16] Li C, Tőkési K, Repetto L, et al. A Monte Carlo calculation of the secondary electron emission in the backward direction from a SiO2 macro-capillary. Eur Phys J D. 2020;74(2):37. doi: 10.1140/epjd/e2020-100268-6

[17] Ding ZJ, Li C, Da B, et al. Charging effect induced by electron beam irradiation: a review. Sci Technol Adv Mater. 2021;22(1):932–971. doi: 10.1080/14686996.2021.1976597

[18] Da B, Liu JW, Yamamoto M, et al. Virtual substrate method for nanomaterials characterization. Nat Commun. 2017;8(1):1–9. doi: 10.1038/ncomms15629

[19] Da B, Liu JW, Harada Y, et al. Observation of plasmon energy gain for emitted secondary electron in vacuo. J Phys Chem Lett. 2019;10(19):5770–5775. doi: 10.1021/acs.jpclett.9b02135

[20] Da B, Liu X, Gong JM, et al. Emitted secondary electrons: in vacuo plasmon energy gain observation using a three-point probe method. Appl Surf Sci. 2022;596:153616. doi: 10.1016/j.apsusc.2022.153616

[21] Howie A, Whelan MJ. Diffraction contrast of electron microscope images of crystal lattice defects-ii. The development of a dynamical theory. Proc R Soc A Math Phys Eng Sci. 1961;263:217–237.

[22] Crimp MA. Scanning electron microscopy imaging of dislocations in bulk materials, using electron channeling contrast. Microsc Res Tech. 2006;69(5):374–381. doi: 10.1002/jemt.20293

[23] Gutierrez-Urrutia I, Zaefferer S, Raabe D. Electron channeling contrast imaging of twins and dislocations in twinning-induced plasticity steels under controlled diffraction conditions in a scanning electron microscope. Scr Mater. 2009;61(7):737–740. doi: 10.1016/j.scriptamat.2009.06.018

[24] Ruan Z, Zeng RG, Ming Y, et al. Quantum-trajectory Monte Carlo method for study of electron–crystal interaction in STEM. Phys Chem Chem Phys. 2015;17(27):17628–17637. doi: 10.1039/C5CP02300A

[25] Kriaa H, Guitton A, Maloufi N. Fundamental and experimental aspects of diffraction for characterizing dislocations by electron channeling contrast imaging in scanning electron microscope. Sci Rep. 2017;7(1):9742. doi: 10.1038/s41598-017-09756-3

[26] Hata S, Furukawa H, Gondo T, et al. Electron tomography imaging methods with diffraction contrast for materials research. Microsc. 2020;69(3):141–155. doi: 10.1093/jmicro/dfaa002

[27] Cheng L, Yang LH, Zeng RG, et al. Theoretical perspective of atomic resolution secondary electron imaging. J Phys Chem C. 2021;125(19):10458–10472. doi: 10.1021/acs.jpcc.1c01382

[28] Da B, Cheng L, Liu X, et al. Cylindrically symmetric rotating crystals observed in crystallization process of InSiO film. Sci Technol Adv Mater: Methods. 2023;3(1):2230870. doi: 10.1080/27660400.2023.2230870

[29] Bolotov IE, Kolosov VY, Kozhyn AV. Electron microscope investigation of crystals based on bend-contour arrangement II. Bending phenomena of the crystal growth in an amorphous film. Phys Status Solidi A. 1982;72(2):645–654. doi: 10.1002/pssa.2210720226

[30] Kolosov VY, Schwamm CL, Gainutdinov RV, et al. Combined AFM-TEM studies of amorphous-crystalline transformation and interface in thin films of Se and Fe2O3. J Phys Conf Ser. 2008;100(8):082037. doi: 10.1088/1742-6596/100/8/082037

[31] Bagmut AG, Grigorov SN, Zhunchkov VA, et al. Morphology and conjugation of nanocrystals growing in Cr-O and VO amorphous films during annealing. Russ Phys J. 2007;50(11):1071–1078. doi: 10.1007/s11182-007-0157-6
[32] Kolosov VY, Schwamm CL, Steeds JW. TEM of lattice bending in crystallized areas of anodized Ta-O films. J Phys Conf Ser. 2008;100(8):082038. doi: 10.1088/1742-6596/100/8/082038
[33] Kolosov VY, Veretennikov LM, Startseva YB, et al. Electron microscopy study of a chalcogenide-based polycrystalline condensate microstructure: the effect of composition and thickness on internal lattice bending. Semiconductors. 2005;39(8):955–959. doi: 10.1134/1.2010692
[34] Richter S, Schwedt A, editors. EMC 2008: materials science. Vol. 2. Berlin: Springer; 2008. p. 343.
[35] Williams DB, Carter CB. Transmission electron microscopy: a textbook for materials science. (NY): Plenum Press; 1996.
[36] Igami Y, Michibayashi K. Transmission Kikuchi diffraction study of submicrotexture within ultramylonitic peridotite. Phys Chem Min. 2021;48(10):38. doi: 10.1007/s00269-021-01161-7
[37] Niessen F, Burrows A, da Silva Fanta AB. A systematic comparison of on-axis and off-axis transmission Kikuchi diffraction. Ultramicroscopy. 2018;186:158–170. doi: 10.1016/j.ultramic.2017.12.017
[38] Kossel W, Möllenstedt G. Elektroneninterferenzen im konvergenten Bündel. Ann Phys. 1939;428(2):113–140. doi: 10.1002/andp.19394280204
[39] Shechtman D, Blech I, Gratias D, et al. Metallic phase with long-range orientational order and no translational symmetry. Phys Rev Lett. 1984;53(20):1951–1953. doi: 10.1103/PhysRevLett.53.1951
[40] Levine D, Steinhardt PJ. Quasicrystals: a new class of ordered structures. Phys Rev Lett. 1984;53(26):2477–2480. doi: 10.1103/PhysRevLett.53.2477
[41] Levine D, Steinhardt PJ. Quasicrystals II. Unit-cell configurations. Phys Rev B. 1986;34(2):596–616. doi: 10.1103/PhysRevB.34.596
[42] Mackay AL. Crystallography and the Penrose pattern. Phys World. 1982;19:22–24.
[43] Senechal M. Quasicrystals and geometry. Cambridge: Cambridge University Press; 1996.
[44] Steurer W. Quasicrystals: what do we know? What do we want to know? What can we know? Acta Crystallogr A. 2012;68:434–448.
[45] Roth J, Clackson S. An ideal spherical crystal: geometrical and structural aspects. J Appl Crystallogr. 1992;25(4):536–536. doi: 10.1107/S0021889892004308
[46] Cheng L, Ming Y, Ding ZJ. Bohmian trajectory-Bloch wave approach to dynamical simulation of electron diffraction in crystal. New J Phys. 2018;20(11):113004. doi: 10.1088/1367-2630/aae8f1
[47] Cheng L, Ding ZJ. Novel quantum trajectory approaches to simulation of electron backscatter diffraction. E-J Surf Sci Nanotech. 2020;18:121–125. doi: 10.1380/ejssnt.2020.121
[48] Venables JA, Spiller GDT. Nucleation and growth of thin films. In: Vu TB, editor. Surface mobilities on solid materials. Boston: Springer; 1983. p. 341–404.
[49] Evans JW, Thiel PA, Bartelt MC. Morphological evolution during epitaxial thin film growth: formation of 2D islands and 3D mounds. Surf Sci Rep. 2006;61(1–2):1–128. doi: 10.1016/j.surfrep.2005.08.004
[50] Shigeto K, Kizu T, Tsukagoshi K, et al. Radial interference contrast in in-situ SEM observation of metal oxide semiconductor film crystallization. Microsc Microanal. 2017;23(S1):1512–1513. doi: 10.1017/S1431927617008224
[51] Gonzalez D, Kelleher JF, da Fonseca JQ, et al. Macro and intergranular stress responses of austenitic stainless steel to 90 strain path changes. Mater Sci Eng A. 2012;546:263–271. doi: 10.1016/j.msea.2012.03.064
[52] Zhou S, Antoja-Lleonart J, Nukala P, et al. Crystallization of GeO2 thin films into α-quartz: from spherulites to single crystals. Acta Mater. 2021;215:117069. doi: 10.1016/j.actamat.2021.117069
[53] Fedchenko O, Winkelmann A, Medjanik K, et al. High-resolution hard-x-ray photoelectron diffraction in a momentum microscope—the model case of graphite. New J Phys. 2019;21(11):113031. doi: 10.1088/1367-2630/ab51fe
[54] Kolosov VY, Thölen AR. Transmission electron microscopy studies of the specific structure of crystals formed by phase transition in iron oxide amorphous films. Acta Mater. 2000;48(8):1829–1840. doi: 10.1016/S1359-6454(99)00471-1
[55] Goh KW, Johan MR, Wong YH. Enhanced structural properties of In2O3 nanoparticles at lower calcination temperature synthesised by co-precipitation method. Micro & Nano Lett. 2018;13(2):270–275. doi: 10.1049/mnl.2017.0540
[56] Nye JF. Some geometrical relations in dislocated crystals. Acta Mater. 1953;1(2):153–162. doi: 10.1016/0001-6160(53)90054-6
[57] Konijnenberg PJ, Zaefferer S, Raabe D. Assessment of geometrically necessary dislocation levels derived by 3D EBSD. Acta Mater. 2015;99:402–414. doi: 10.1016/j.actamat.2015.06.051
[58] Callister WD Jr. Fundamentals of materials science and engineering. Danvers (MA): John Wiley & Sons, Inc.; 2005.
[59] Dasari SG, Nagaraju P, Yelsani V, et al. Nanostructured indium oxide thin films as a room temperature toluene sensor. ACS Omega. 2021;6(27):17442–17454. doi: 10.1021/acsomega.1c01831